Nuclear Instruments and Methods in Physics Research A 859 (2017) 102–111

Contents lists available at ScienceDirect

Nuclear Instruments and Methods in Physics Research A

journal homepage: www.elsevier.com/locate/nima

A high-compression electron gun for C^{6+} production: concept, simulations and mechanical design

Robert Mertzig[a,b], M. Breitenfeldt[a], S. Mathot[a], J. Pitters[a,d], A. Shornikov[c,1], F. Wenander[a,*]

[a] CERN, Geneva 23, CH-1211, Switzerland
[b] Technische Universität Dresden, Dresden 01069, Germany
[c] The University of Manchester, Manchester, M13 9PL, UK
[d] Technische Universität Wien, 1040 Vienna, Austria

ARTICLE INFO

Keywords:
EBIS, EBIT
Brillouin electron gun
Ion sources
Hadron therapy
Highly charged ions

ABSTRACT

In this paper we report on simulations and the mechanical design of a high-compression electron gun for an Electron Beam Ion Source (EBIS) dedicated for production of high intensity and high repetition rate pulses of bare carbon ions for injection into linac-based hadron therapy facilities. The gun is presently under construction at CERN to be retrofitted into the TwinEBIS test bench for experimental studies. We describe the design constraints, show results of numeric simulations and report on the mechanical design featuring several novel ideas. The reported design makes use of combined-function units with reduced number of mechanical joints that were carefully controlled and tuned during the manufacturing phase. The simulations addressed a wide range of topics including the influence of thermal effects, focusing optics, symmetry-breaking misalignments and injection into a full 5 T field.

1. Motivation

In the last two decades radiotherapy with ion beams has made substantial progress and established itself as a superior method for treatment of a variety of cancer types. A beam of ions compared to X-ray or electron irradiation provides a more targeted dose delivery owing to the finite range in combination with a pronounced Bragg peak in energy deposition. In clinical trials [1] it was found that certain types of cancer are resistant to both X-ray and proton irradiation and are curable only if heavier ions, such as carbon, produce many closely located double-strand DNA breakups in the irradiated tumor [2]. The magnetic rigidity of the heavier ions and the higher energy required to attain the same penetration depth in the body, have made Light Ion Therapy (LIT) facilities expensive both in terms of construction and operation [3].

Several new accelerator designs were suggested in order to reduce construction and operation costs of LIT facilities by using simpler design, reduced geometric footprint, and lower required maintenance. Progress in other technologies such as recent advances in superconducting gantries [4,5] also contribute to achieving economic sustainability of LIT.

As discussed in [6] among the new LIT accelerator designs only linac-based schemes such as high frequency linacs [7] and cyclotron +linac booster combinations (cyclinac [8–10]) are technologically mature and offer attractive balance of treatment quality and costs. The operation of both types is hindered by the lack of a suitable C^{6+} source providing pulses of the required structure: 300–400 Hz repetition rate, 10^8 C^{6+} within 1.5 μs (FWHM) pulse length [8] and specified beam purity. The general requirements to the ion pulse structure (short, intense, high repetition rate) make an EBIS an ion source of choice for linac and cyclinac concepts [6]. At the same time, achieving the specific design values for linac and cyclinac injection is not possible for modern EBISes [6] due to insufficient ion pulse intensity or pulse repetition rate. Both parameters are defined by the electron beam optics of the EBIS. Simultaneously pushing the capacity and repetition rate to linac-based LIT specifications require substantial design efforts to create a dedicated EBIS providing a highly compressed and intensive electron beam at low energy, ideally suited for ionisation and confinement of bare carbon ions.

In this paper we report on design and simulation results of a new electron beam optics, called MEDeGUN, to be retrofitted in the existing TwinEBIS at CERN. The electron gun is presently under construction and aims to bridge the gap between high intensity low repetition EBISes and low intensity high repetition Electron Beam Ion Traps, thus creating a C^{6+} source for linac-based LIT facilities [6].

* Corresponding author.
E-mail address: fredrik.wenander@cern.ch (F. Wenander).
[1] Present address: GANIL, Bd. Becquerel, BP 55027, 14076 Caen Cedex 05, France.

http://dx.doi.org/10.1016/j.nima.2016.12.036
Received 11 November 2016; Received in revised form 18 December 2016; Accepted 21 December 2016
Available online 11 January 2017

2. Design parameters

In the EBIS design the electron beam is extracted from a cathode, focused electrostatically by the Wehnelt electrode and anode, and injected into a magnetic field where the maximum current density is achieved. At the other side of the solenoid the electron beam is recovered on a collector electrode.

The prerequisites on the electron beam optics, arising from using the EBIS for a LIT-injector, will be discussed here. In the motivation section three key parameters for the LIT-injector were listed: extraction time of approximately 1.5 μs; ion intensity of 10^8 C^{6+} per pulse and pulse repetition rate of 300–400 Hz. The forth, i.e. the beam contamination, is discussed in [6]. In an EBIS high charge states are achieved by consecutive electron impact ionisation, competing with radiative electron recombination, while charge exchange effects are small as the vacuum is in the order of 10^{-10} mbar. Knowing the cross-sections of these processes, the evolution of the Charge State Distribution (CSD) can be numerically simulated [11].

2.1. Parameter relations

For practically interesting electron energies the abundance of bare carbon in the CSD at a given breeding time decreases with the electron energy (compare 5 keV and 10 keV operation in Fig. 1), favoring operation at a lower energy. The 1.5 μs pulse length criterion can be translated into an ion trap size not exceeding L=0.25 m, for which similar extraction times have been demonstrated [12]. An extraction efficiency factor of γ=0.5 has to be applied to account for ions not fitting within the extraction time window in spite of the short trapping region.

The intensity criterion of carbon ions injected into LIT can be treated as follows. For electron energies E_e in the range 4–10 keV the carbon CSD is calculated. For several selected electron current densities in the range of j_e=0.5–3.5 kA/cm^2 the corresponding C^{6+} abundances $A(E_e, j_e, \tau)$ after a breeding time τ=2.5 ms for a given E_e and j_e are determined. Finally, the electron current I_R required to achieve C=10^8 C^{6+} ions injected into the LIT accelerator is calculated assuming that L=0.25 m, γ=0.5 and the total positive charge of carbon ions equals only 10% of the electron space charge, i.e. a carbon partial neutralisation factor f of 0.1. The required current $I_R(E_e, j_e)$ is then equal to:

$$I_R(E_e, j_e) = \frac{qC(e\sqrt{2E_e/m_e})}{Lf\gamma A(E_e, j_e, \tau)} \quad (1)$$

where q is a weighted average carbon charge state, e the elementary charge and m_e the electron mass. The calculated $I_R(E_e)$ dependency for selected j_e are shown in Fig. 2.

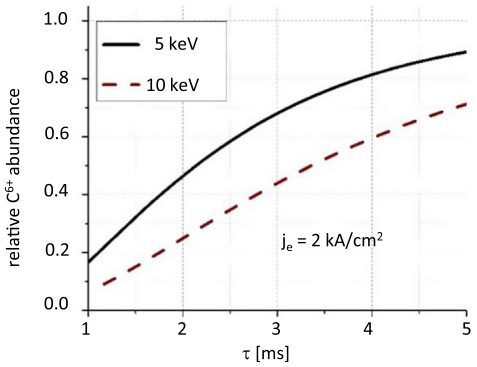

Fig. 1. Relative abundance $A(E_e, j_e, \tau)$ of C^{6+} as function of breeding time τ for two electron beam energies E_e. The current density j_e was 2 kA/cm^2 in both cases. The abundance has been calculated using the CBSIM code [11].

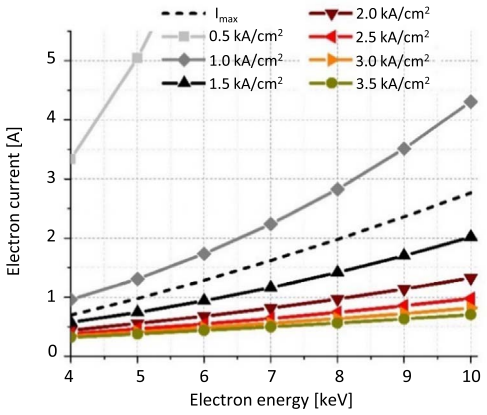

Fig. 2. The required electron beam current I_R as function of electron beam energy E_e for electron densities j_e=0.5–3.5 kA/cm^2.

2.2. Perveance limit

The electron space charge limits the maximum transportable electron current I_{max} at a given electron energy as $I_{max}=p_{max}(E_e/e)^{1.5}$, where p is the perveance. For an annular beam with the same radius as the enclosing drift tube the maximum perveance is ~$32.4\cdot10^{-6}$ $AV^{-1.5}$ [13]. In everyday EBISes the ratio of beam radius r_b to the drift tube radius r_{dt} is in the range 50–100. If $2\ln(r_{dt}/r_b) > > 1$ the maximum attainable perveance p_{max} can be approximated [13] as:

$$p_{max} = \frac{25.\ 4\cdot10^{-6}}{1 + 2\ln\left(\frac{r_{dt}}{r_b}\right)} \quad (2)$$

For r_{dt}/r_b=60 the maximum current $I_{max}=p_{max}(E_e/e)^{1.5}$ is plotted amid the $I_e(E_e, j_e)$ curves in Fig. 2. Only current densities exceeding 1.2 kA/cm^2 allow to maintain I_R smaller than I_{max}.

2.3. Design parameter summary

In order to have sufficient safety margin in case of any imperfections and inaccuracy in the simulations we have set our goal for the 5 T beam compression about twice higher than is necessary for a LIT-injector. Such significant safety margin comes from the reports of similar devices failing to meet the simulated predictions.

Applying the same analysis as in [14] using MEDeGUN parameters demonstrated that instability may be a threat at current densities below 4.3–4.9 kA/cm^2 in the absence of other sources of extra transverse energy. By keeping an option of a current density in the operating source in excess of 5 kA/cm^2 a precaution against plasma instabilities, possibly present at lower densities, is taken.

The required current density significantly exceeds achievable with immersed-flow guns operating with the same magnetic field. Hence, we have chosen to proceed with a Brillouin-flow electron gun type. Based on the considerations mentioned above we can summarise our design goals for the electron gun as follows: the electron current should be 1 A, with a beam energy between 7.5 and 10 keV and attain a current density of 3.5 kA/cm^2 in a breeding region with a field of 5 T. The electron gun will first be tested at the TwinEBIS setup which is based on a 2 T magnet. Provided no plasma instabilities occur, the electron gun is in principle capable of operating at a main solenoid field of 2 T and still provide a sufficient current density of 1.5 kA/cm^2.

3. Electron gun and beam simulation results

In this section the results from numerical simulations of MEDeGUN are discussed. The general design was influenced by earlier works on high-compression electron guns [15,16]. The central gun

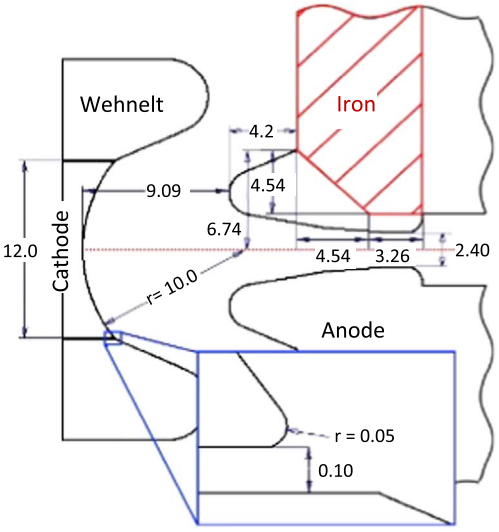

Fig. 3. Electron gun geometry. Electrostatic (black) and magnetic (hatched red) components together with dimensions in mm. (For interpretation of the references to color in this figure legend, the reader is referred to the web version of this article.)

geometry is given in Fig. 3, showing the electrostatic parts consisting of cathode, Wehnelt and anode electrodes, and the ARMCO™ iron shield. The latter is used to screen the gun volume from the magnetic field originating from the main solenoid. The iron shield furthermore generates the required field gradient shape for injection into the main magnetic field [17]. Being a full-scale prototype for a LIT-injector also means the gun is designed for heavy-duty long-term operation. As such it features a large cathode of 12 mm diameter operating with a low current density, which should guarantee sufficient lifetime and reduced beam aberrations that otherwise could be caused by local variations in the work function or cathode surface irregularities.

In order to perform electron beam simulations beyond the magnetically shielded MEDeGUN volume and study the beam in a high magnetic field we have extended the simulation domain adding the 2 T solenoid of TwinEBIS, as shown in Fig. 4, and used a simulation approach described in [18].

3.1. Magnetic field in the gun region

The iron shield surrounding the electron gun suppresses the magnetic field from the main solenoid, both for 2 T and 5 T, down to a level of 0.1 mT at the cathode surface to allow for an electrostatic compression inside the gun. Two coils, the gun and anode coils, are used to shape the magnetic field in the vicinity of the electron gun, as illustrated in Fig. 5a. The gun coil compensates for the homogenous

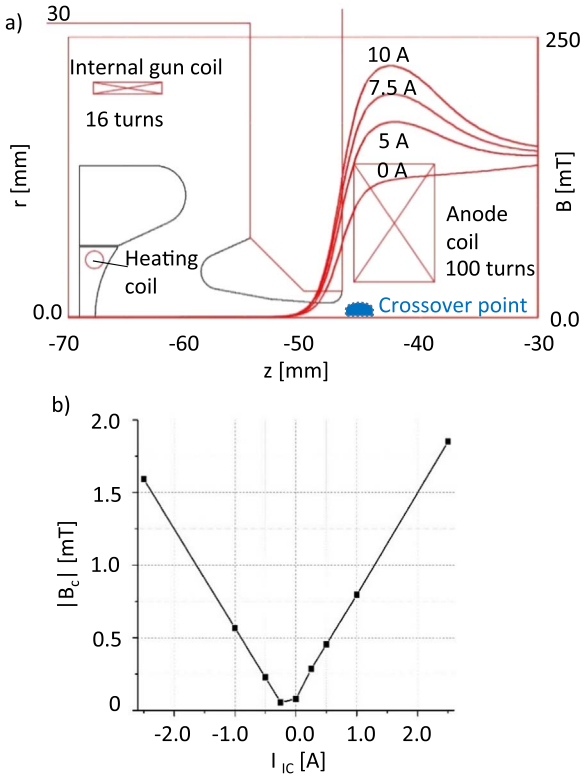

Fig. 5. a) Layout of the internal gun coil and anode coil overlaid with the axial magnetic field for different currents I_{AC} in the anode coil. b) Simulation of the combined magnetic field $|B_C|$ from the internal gun coil and the solenoid at the centre of the cathode surface as function of excitation current I_{IC} in the internal gun coil.

residual magnetic field at the cathode surface. In Fig. 5b the total magnetic field $|B_C|$ including respective contributions from the main solenoid and the gun coil is plotted as a function of excitation current I_{IC} in the gun coil. A current of −0.1 A is required to counterbalance the residual field strength from the solenoid. The anode coil shapes the magnetic field in the crossover point B_{CO}, as shown in Fig. 5a. The polarity of the excitation current I_{AC} of the anode coil can be reversed to decrease the magnetic field B_{CO}. The nominal magnetic field in the crossover point is 0.14 T for a 1 A and 10 keV electron beam and is achieved with 0 A in the anode coil with the electron gun at its nominal axial position. When the gun voltage is increased, the current density in the crossover point j_e^{co} increases too. The optimal magnetic field for a cold electron beam at the crossover point B_{CO} can be approximated with [17]:

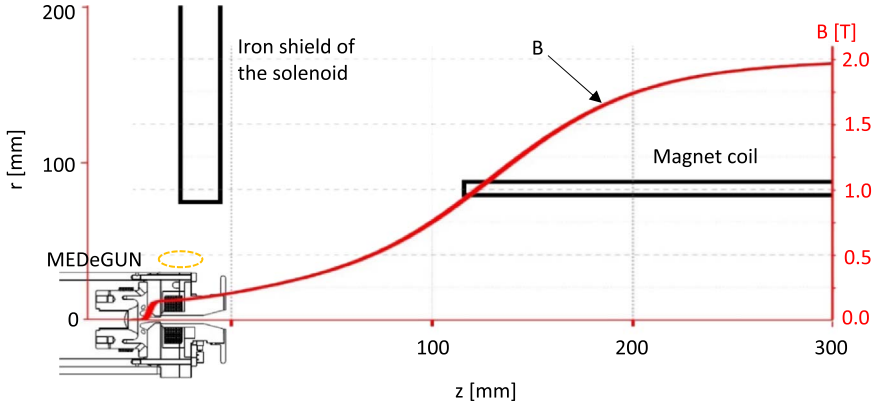

Fig. 4. Magnetic field inside the TwinEBIS solenoid with MEDeGUN inserted. The graph shows the B_z component of the magnetic field along the axis. The dashed ellipse indicates the region with the highest probability for magnetron discharges. Radial direction of electron gun not to scale.

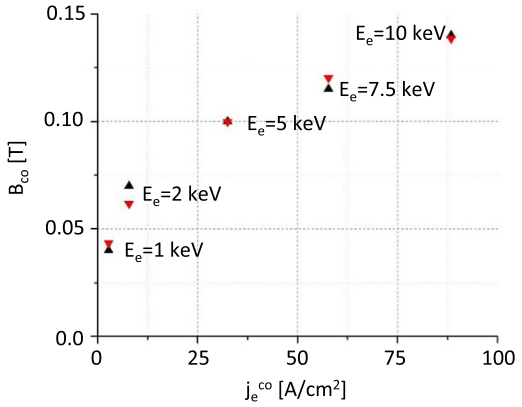

Fig. 6. Simulated optimal magnetic field at the crossover point for different gun voltages (up-pointing triangles) and the optimal matching field according to Eq. (3) (down-pointing triangles), taking j_e from the beam simulations. The uniformity of the phase space in the crossover point was used as a quality factor to establish the optimal magnetic field during the simulations.

$$B_{co} = \sqrt{\frac{\pi j_e^{co}}{C_1\sqrt{E_e}}} \tag{3}$$

where C_1=145 $cm^2eV^{1/4}A^{-1/2}T^{-2}$ and current density j_e, electron beam energy E_e and magnetic field are in units of A/cm^2, eV and T, respectively. In Fig. 6 the optimal magnetic field in the crossover point is plotted for different gun voltages. The intended tuning procedure is to move the gun axially in order to optimise the magnetic field, which can thereafter be fine-tuned with the anode coil.

3.2. Wehnelt potential

In previous work on the high-compression electron gun HEC^2 [19] it was shown that the electrons emitted from the cylindrical side surface of the cathode will partly be reflected by the magnetic field gradient and cause loss current on the anode. Applying a negative bias to the Wehnelt electrode in the order of a few per mille of the cathode-anode voltage allows to minimise the extraction of side-emitted electrons, at the cost of aberrated trajectories emitted from the front surface close to the cathode rim. In the design of the MEDeGUN the gap between the cathode and the Wehnelt is reduced to 0.1 mm to mitigate the penetration of the extraction field into the gap. Owing to the smaller gap compared to HEC^2 a Wehnelt bias of only 7 V is needed for a cathode bias of 10 kV. Wehnelt bias voltages significantly higher than 7 V cause over-focusing and introduce unwanted transverse momenta. Fig. 7 shows results from electron beam simulations using Field Precision TRAK [20].

3.3. Cathode temperature influence on beam propagation

As part of the simulation studies we wanted to assure that the thermal effects often omitted in gun designs will not create any significant unwanted disturbance to the beam optics. The built-in feature in the simulation software that emulates emission from a non-zero temperature cathode was used, assuming a cathode temperature of 1273 K (0.11 eV). The influence of temperature related effects in the gun region can be seen in Fig. 8. The horns at the edge of the beam, especially well seen for T=0 K, are typical for focused Brillouin electron beams of uniform work function at the cathode. The horns become less pronounced with larger radial tails instead when the electron temperature is taken into account. In high magnetic field the beam has a Gaussian density distribution in radial direction [17]. The larger radial size and the increased transverse momentum from thermal effects have a major impact on the beam emittance. The normalised emittance at the crossover point calculated from the results of the beam tracing changes from 0.9 to 5.5 μm when thermal effects are included. The emittances are radial RMS emittances [21] calculated as:

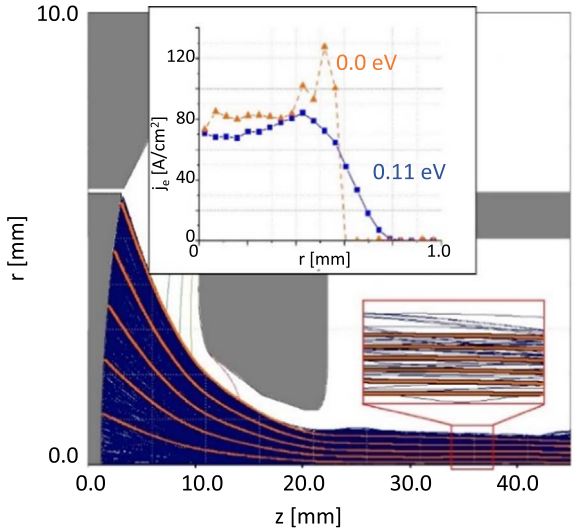

Fig. 8. Simulated electron trajectories in the electron gun region. The orange lines show the beam without the thermal effects (only each 30th trajectory is shown). The blue trajectories are calculated with 1273 K emission temperature (0.11 eV). The same colour coding applies to the inserts showing the current density distribution (top) across the beam at the position of the enlarged segment (bottom).

$$\varepsilon_r = \beta\gamma \quad 2\times\sqrt{\langle r^2\rangle[\langle(p_r/p_z)^2\rangle + \langle(p_\theta/p_z)^2\rangle] - \langle rp_r/p_z\rangle^2 - \langle rp_\theta/p_z\rangle^2} \tag{4}$$

where < > denotes averaging, r is the radius, p_r, p_z, p_θ are the momentum components, $\gamma = 1/\sqrt{1-\beta^2}$ and $\beta=v_{tot}/c$ with c as the speed of light.

3.4. Cathode surface roughness

Cathode surfaces have a certain roughness due to the limits of the manufacturing processes. Electrons starting from an uneven surface

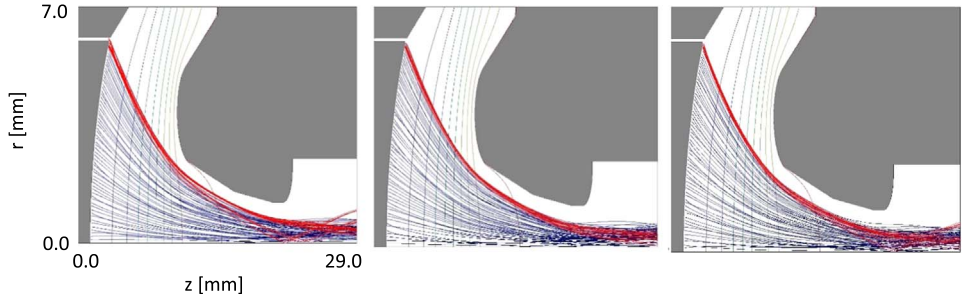

Fig. 7. Electron beam propagation in the gun volume for different Wehnelt voltages. Trajectories emitted close to the cathode rim are shown in red. From left to right: Wehnelt bias of 0 V, 7 V and 20 V. The beam current is 1 A at an extraction voltage of 10 kV. (For interpretation of the references to color in this figure legend, the reader is referred to the web version of this article.)

create local areas of higher and lower electron densities, which act as lenses, and consequently add additional transverse momentum to the electrons [22]. In order to estimate the effect one can compare the surface roughness with the distance between the cathode and the potential minimum in front of the cathode surface. The potential difference U-U_{min} between the cathode and the potential minimum can be approximated with the equation [23]:

$$(U - U_{min}) = \frac{T_c}{C_2} log\left(\frac{j_e^{max}}{j_e}\right) \quad (5)$$

where C_2 =5040 KV^{-1}, j_e^{max} is the maximum cathode current density for a certain cathode temperature T_c and j_e is the operational current density. The potential difference is used to calculate the distance between the cathode and the potential minimum Δz as:

$$\Delta z = \sqrt{\frac{4\varepsilon_0}{9}\left(\frac{2e}{m_e}\right)\frac{(U - U_{min})^{1.5}}{j_e}\left[1+\sqrt{C_3\frac{T_c}{(U - U_{min})}}\right]} \quad (6)$$

with C_3 =0.000625 VK^{-1}. The additional transverse energy due to the surface roughness equals approximately e(U-U_{min}) if the surface roughness is similar to Δz. At an operational temperature of 1273 K the maximal current density j_e^{max} is expected to be ~3 A/cm^2, while the design value for the MEDeGUN cathode current density j_e is 1 A/cm^2. These numbers give a U-U_{min} and Δz of 0.12 V and 6 μm, respectively. The cathode roughness has been specified to be < 1 μm. Based on these numbers, and assuming a linear scaling, an additional transverse temperature of less than 0.02 eV is anticipated. A non-uniform work function across the cathode surface can in the same way as the surface roughness introduce additional transverse momenta to the electrons. Operating the cathode well into the space charge limited region, i.e. at a temperature capable of providing a higher current density than can actually be extracted, mitigates the risks of non-uniform emission due to local temperature differences and non-uniform work function.

3.5. Alignment and manufacturing tolerances

For manufacturing purposes the influence of various mechanical and field misalignments on the beam properties were investigated. For instance, the inclination of the Wehnelt surface (α) and the angle of the anode opening (β) have been varied in the range of ±2 degrees from their optimal design values. Fig. 9 demonstrates the variation of the Wehnelt and anode shapes. Furthermore, the axial positioning (Δz) of the cathode was scanned relative to the Wehnelt electrode by up to −0.3 mm. In Fig. 10 the minimal distance between electron beam and anode d_{min} and the emittance are plotted versus angular variations and axial displacement. The correct axial positioning of the cathode is crucial for the beam quality of MEDeGUN, as well as the inclination of the Wehnelt shape. It was found that by retracting the cathode by 0.1 mm, the safety distance between the electron beam and the anode electrode increased, at the cost of moderate increase of transversal energy spread, while a further displacement deteriorates the beam quality, see Fig. 11. In addition, the amount of extracted side-emitted

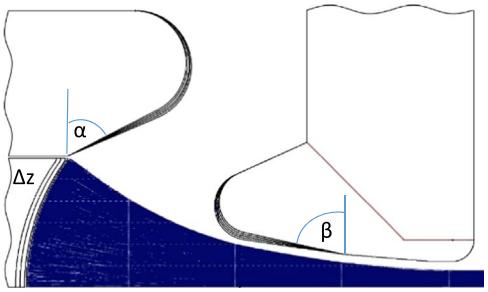

Fig. 9. Varied geometrical parameters for establishment of manufacturing tolerances: cathode displacement Δz, Wehnelt shape α and anode shape β.

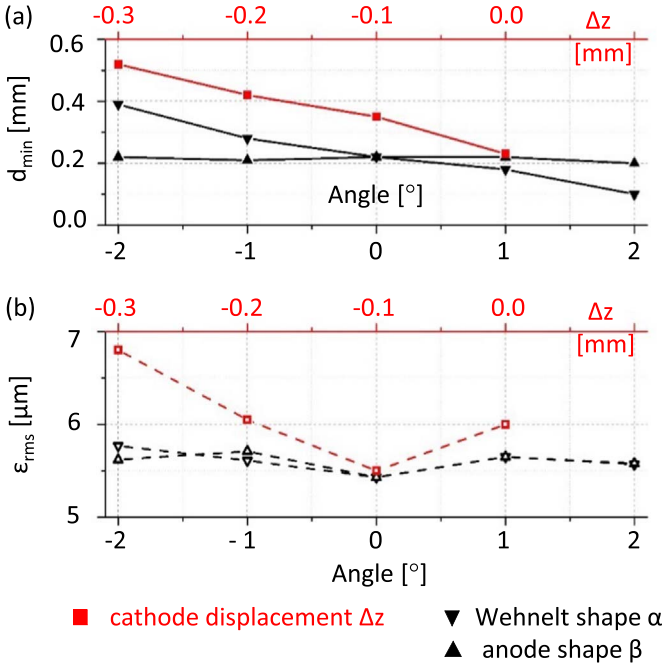

Fig. 10. Minimal distance between electron beam and anode (a) and emittance in the crossover point (b) when varying the cathode position axially as well as the Wehnelt and anode shapes.

electrons for any given Wehnelt bias is also reduced. Thus, the 0.1 mm retracted position has been taken as the default design. If the cathode and Wehnelt electrode are displaced radially relative to the anode, mainly beam steering occurs. The result of a 3D simulation for 0.1 and 0.3 mm displacement is shown in Fig. 12. For a radial misalignment of 0.3 mm part of the electron beam hits the anode. Along with this direct loss current, the electron beam gains additional transverse momentum, which lowers the probability of acceptance by the main solenoid. Finally, the electron beam injection into the full 5 T field was simulated. The task is demanding because the electron beam diameter shrinks from 12 mm at the cathode to 100 μm when fully compressed. Providing the necessary uniformity of spatial resolution throughout the entire volume is impossible for any standard simulation program. Hence, an earlier developed technique [18] of dividing the geometry axially into sub-domains was employed. The tracing was organised using 14 sub-domains, where the magnetic field increases from the injection field of 0.14 T to 5 T in steps of 0.4 T, such that in each sub-domain an adequate number of mesh cells and mesh quality is maintained. The total energy conservation for the simulated trajectories was at a level of 99.85%. The traced beam was generated with optimal Wehnelt voltage and with thermal effects included. A total of 204 emission nodes, each split into 5 thermal trajectories, were traced yielding a total of 1020 trajectories. No reflected trajectories were observed. For the outermost trajectories with excessive transverse momentum an increase of the field to 5.8 T will cause reflection due to the magnetic mirror effect. The magnetic compression safety factor is 190% for 2 T operation and only 16% for 5 T operation. The local current density through the magnetic compression part is shown in Fig. 13. The radius of the simulated electron beam containing 80% of the current equals 60(±3) μm and agrees within two σ with the theoretically calculated Herrmann beam radius of 54 μm. According to the simulations the beam encompassing 80% of the current will have an average density of 7.5 kA/cm^2 giving us a safety margin of a factor 2 compared to our design goal of 3.5 kA/cm^2. The current density resulting from the calculated Herrmann beam radius is 8.8 kA/cm^2. Because of the space charge potential from the electron beam itself, the energy in the crossover point at 0.14 T will be 9.3 keV and ~8 keV on the beam axis in the trapping region at 5 T.

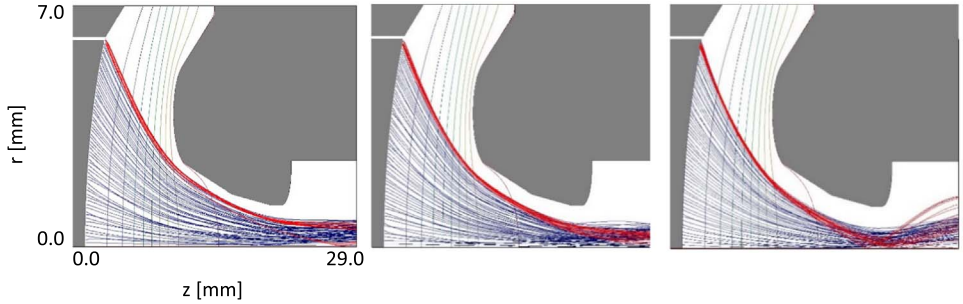

Fig. 11. Electron beam propagation in the gun volume for different axial cathode displacement with respect to the Wehnelt electrode; from left to right Δz =0, −0.1 and −0.3 mm. For Δz =−0.1 mm displacement the most advantageous trade-off between parallel beam trajectories and safety distance between the anode and electron beam is found. Optimum Wehnelt bias of −7 V applied in all three cases.

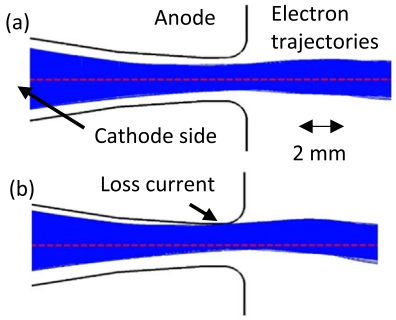

Fig. 12. 3D simulation of an electron beam in the vicinity of the anode. In the 2D projections the cathode and Wehnelt electrodes are radially displaced by 0.1 mm (a) and 0.3 mm (b) relative to the anode hole and iron shield.

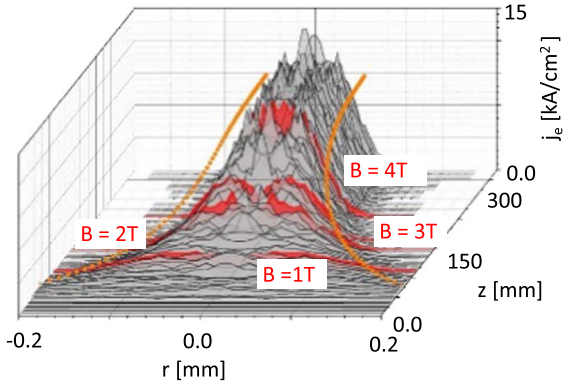

Fig. 13. Magnetic compression of the beam into a 5 T magnetic field. The beam current is 1 A for a cathode-to-anode voltage of 10 kV, corresponding to a beam energy of ~8 keV in the trapping region. The current density at the calculated Herrmann beam diameter (containing 80% of the beam current) is shown by orange dotted lines. (For interpretation of the references to color in this figure legend, the reader is referred to the web version of this article.)

Table 1
Electron gun characteristics and simulated performance.

Parameter	Value	Remarks
Full design voltage	10000 V	
Full design current	1 A	
Perveance	1×10^{-6} AV$^{-1.5}$	
Current density 2 T / 5 T	3.1 / 7.5 kA/cm^2	Defined within 80% of the current
Kilpatrick safety factor	3.85	
Magnetic compression safety factor 2 T / 5 T	190% / 16%	
Normalised emittance at crossover for T=0 K	0.9 μm	rms emittance neglecting thermal effects
Normalised emittance at crossover for T=1273 K	5.5 μm	rms emittance including thermal effects

The design of the electrostatic part was analysed with respect to electrical discharges. When applying the Kilpatrick criterion [24] a safety factor of 3.85 was found at the most critical point, the Wehnelt, for 10 kV cathode-to-anode voltage. The simulated gun performance is summarised in Table 1.

4. Mechanical realisation

In this section we give an overview of the mechanical design of the electron gun based on both simulation results and the constraints of the test bench.

4.1. The test bench

The MEDeGUN design will be tested at the TwinEBIS setup at CERN [25]. TwinEBIS offers 0.8 m trapping length for the ions. The electron transport through the trap is maintained by an iron-shielded warm-bore 2 T superconducting magnet. For the MEDeGUN tests the TwinEBIS setup will be complemented with a gate valve (see Fig. 14) separating the drift tube region from the electron gun when retracted into the gun chamber, thus allowing gun maintenance without venting the trapping and collector volumes. In the gun and collector regions turbo-molecular drag pumps provide the vacuum, while non-evaporable getter (NEG) strips complement the pumping in the trapping region. Pressures below 10^{-10} mbar are attained. The turbo pumps are connected to a pump stand consisting of a booster turbo pump and a rotary pump.

Electron beam simulations have shown that the TwinEBIS sup-

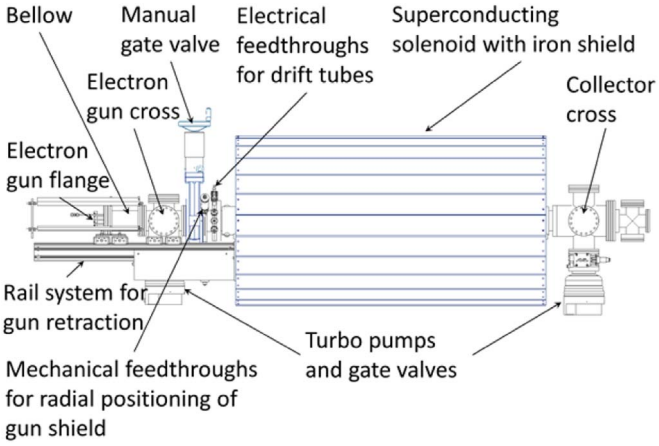

Fig. 14. TwinEBIS setup modified for tests with MEDeGUN. On the left side the gun vacuum cross is separated from the drift tube region with a gate valve. The 350 mm stroke bellow enables the electron gun to be retracted from the drift tube region into the gun vacuum cross. The bellow with the electrical feedthrough flange slide on support rails. The iron shield of the solenoid is shown in the centre, the collector on the right-hand side.

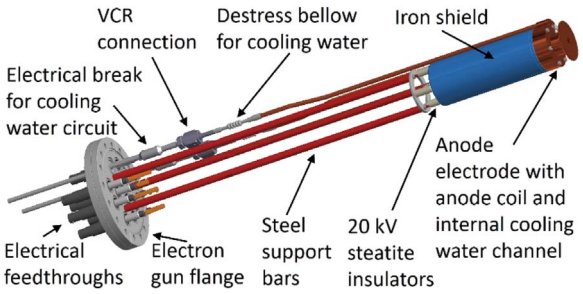

Fig. 15. Electron gun assembly with the electrical feedthrough flange. The iron shield is supported by three stainless steel rods, with steatite insulators inserted allowing the shield and anode to be biased to +5 kV with respect to the vacuum tube. The cooling water is fed in via two copper tubes, with an isolation break and VCR coupling in series.

pressor and collector need to be closer to the main solenoid in order to avoid excessive losses on the non-cooled suppressor and non-optimal power loss distribution on the collector. A move of the suppressor and collector is foreseen.

4.2. Electron gun design

The MEDeGUN is designed according to constraints of the TwinEBIS setup, such as a 2 T magnetic field and 100 mm inner diameter of the vacuum tube. Due to the high-voltage safety distance and the mounting concept of the drift tube structure the diameter of the iron shield surrounding the gun was limited to 60 mm. Two different designs of the anode tube have been prepared (see Fig. 16) as there is a risk of magnetron discharges between the anode tube and the first drift tube.

The magnetic field at the crossover point has to be adjusted for different electron currents. This is accomplished by moving the axial position of the electron gun with respect to the main solenoid. The electron gun assembly with its mounting to the feedthrough flange is laid out in Fig. 15. The length of the support rods has been chosen to allow for a complete retraction of the electron gun into the gun chamber, as well as to reach the optimal magnetic field at the crossover point. A welded bellow with an axial stroke of 350 mm enables the retraction of the gun. The electron gun cross and the sliding end flange with the electrical feedthroughs are mounted on a rail system from ITEM™. Three fine-threaded brass stiffeners prevent the bellow from collapsing by the atmospheric pressure, and assure the radial positioning of the electron gun with respect to the drift tubes and the magnetic field from the main solenoid.

In order to verify the radial position of the gun assembly three linear feedthroughs are installed radially between the gate valve and the vessel of the magnet. When inserted they come in contact with the isolated iron shield. By monitoring when a short circuit occurs between the anode, i.e. the iron shield, and ground, i.e. the linear feedthrough, the position of the iron shield can be established. The feedthroughs are able to register positions with an accuracy of 0.025 mm, far better than required from a beam optics point-of-view.

Special design efforts were made to assure minimum tolerances in the gun assembly. In order to minimise misalignments some parts were manufactured in an unconventional manner, and for any mounting special care was taken about proper alignment guides, manufacturing tolerances, etc. The electrodes surrounding the cathode, i.e. the Wehnelt and anode, are machined to a precision of 20 μm with respect to the optimal solution found in the electron beam simulations. These electrodes in combination with the cathode itself determine the electric field for the electrostatic compression, and thereby the electron current density distribution in the crossover point.

As pointed out in the simulation section, the cathode and the Wehnelt electrode are to be installed concentrically with a separation of 100 μm. Hence the cathode and its mounting have to be machined with the same precision as the Wehnelt and the anode electrodes. The Wehnelt is fixed to the iron shield front plate, and as a result to the anode electrode, with a precision of 20 μm, whereas the alignment of the iron front plate with respect to the cylindrical part of the iron shield is less critical. The iron shield is made of ARMCO™ soft-iron, annealed at 1000 °C to maximise the magnetic permeability at low magnetic fields.

The machining of the central hole in the iron shield is done with respect to its outer diameter. This hole defines the centre of the magnetic field. Attached to the iron shield front piece is the anode. The anode electrode, made of oxygen-free electronic (OFE) copper is brazed to the iron shield, and after-machined with respect to the outer diameter of the iron shield. Thereby the magnetic and electrostatic axes from cathode to anode are concentric. The threaded holes for fixing the Wehnelt to the iron shield and the holes for the fixation of the outer anode electrode are sufficiently far away from the beam axis to not alter the relevant magnetic field. The long cylindrical body of the iron shield prevents magnetic field penetration from the rear. Nevertheless, a low magnetic field may exist inside the iron shield, being a sum of the fields generated by the filament heating current, leaking through the iron shield holes and the actual electron beam current. To counteract this a small 16-turn coil, the internal gun coil, is located at the lateral surface of the Wehnelt piece, see Fig. 16. The anode coil outside the iron shield is meant to adjust the magnetic field gradient. It is situated in the electrode which hosts the cooling water

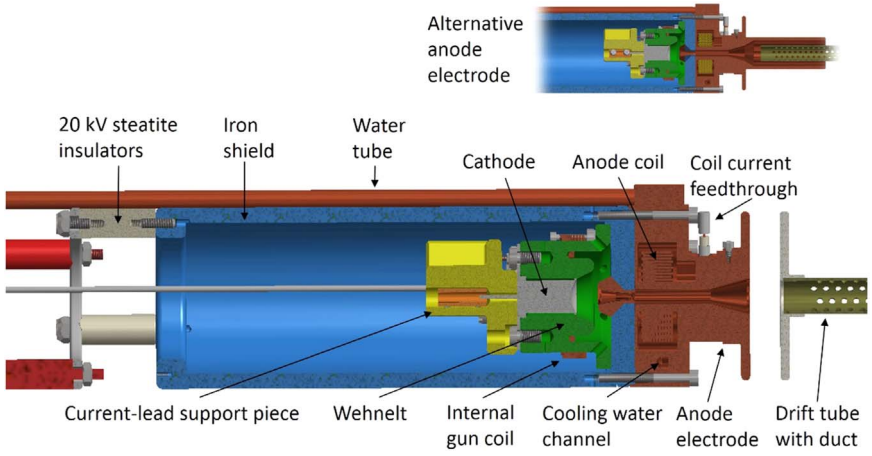

Fig. 16. Cross-section of the electron gun assembly. The iron shield (blue) supports the Wehnelt piece (green), which in turn holds the cathode (grey). With the coils the magnetic field at the cathode and in the crossover point can be adjusted. Due to the risk of magnetron discharges between the anode and the first drift tube two different anode electrode designs are to be compared. (For interpretation of the references to color in this figure legend, the reader is referred to the web version of this article.)

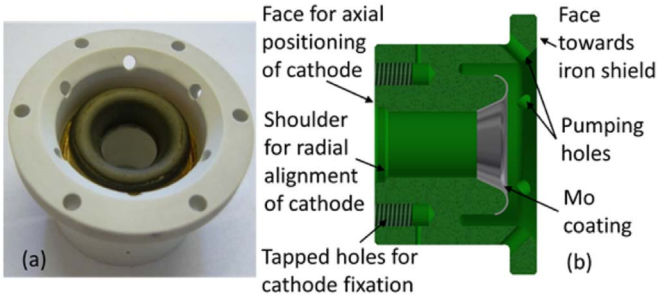

Fig. 17. Wehnelt piece. a) Photo of the Wehnelt piece with molybdenum coating at the Wehnelt electrode surface. b) Cross section along the symmetry plane with indications of the electrode creating coating.

channel, see Fig. 16. The 100 turn coil with an inner diameter of 10 mm is sealed from the vacuum inside a small chamber, with the current being applied via micro feedthroughs. The coil is wound of a custom-made ceramic-coated silver wire with 1 mm diameter and can withstand temperatures of 800 °C for a short time, which may occur locally during the welding process of the enclosing coil chamber.

For reasons of electric and magnetic field alignment the number of mechanical transition have been minimised. Between the cathode and anode only two transitions are present. This has been achieved by merging the central Wehnelt electrode with the insulators separating the electrical potentials towards the cathode and the anode as shown in Fig. 17. In practice it is realised by machining the surface of a single isolator as required by the electric field map and consequently coat part of it with molybdenum to create the actual Wehnelt electrode. The conducting part of the surface is indicated in the cross-section in Fig. 17. The insulation should withstand a potential difference of 15 kV between Wehnelt and anode, as the cathode may be biased with −10 kV and the iron shield to approximately +5 kV. At the rear of the cathode a piece made of Macor™ is placed, which supports the current leads and the electrical connection between the wire and the circular ring that applies the Wehnelt potential.

As material for the insulator Shapal™ Hi-M soft, an aluminium nitride based ceramic, was chosen. Shapal is machinable and has a very high heat conductivity (5 10^{-6} W·K^{-1}m^{-2}). The latter is important as the cathode housed inside the ceramic piece is heated to 1000 °C, and the radiated heat reaching the insulator consequently has to be evacuated. Via the iron shield the insulator is connected to a heat sink provided by a water cooling circuit. The circuit is dimensioned to remove the heating power from the cathode (24 W), the ohmic heating from the two gun coils (together 15 W) and heat deposited on the extended anode electrode (10 W per mA loss current; limit 10 mA). A conservative estimate resulted in a maximum temperature difference of 200 °C between the rear surface, where the cathode is connected, and the front face where the ceramic will be connected to the iron shield which is adjacent to the cooling water circuit. The geometry has been modelled for stress analysis in ANSYS v15 [26]. The simulation resulted in a safety factor for the tension and compression of 2 and 4, respectively.

To prepare the setup for a background vacuum in the order 10^{-10} mbar the gun cross and thus its content will be baked out at 250 °C.

In order to assess the risk of developing magnetron discharges in the gun we have calculated the characteristic radii of cycloids flown by spontaneously emitted electrons in crossed electric and magnetic fields along the gun surface. The ratio R of the cycloid radius to the distance between two parts defines whether the presence of a magnetic field will facilitate the ignition of a discharge (R=1-0.1), has minor influence on it (R > 1) or suppresses the discharge (R«1) by locking electrons close to the surface [27]. For a maximal anode bias of 5 kV there is one potentially unsafe region between the iron shield of the electron gun and the vacuum tube at the axial position of the anode, indicated in Fig. 4. The unavoidable danger comes from the large variation in axial magnetic field along the electron gun. Nevertheless, it is expected that the strong radial magnetic field component may evacuate electrons from the critical region. Our chosen course of actions was to limit the anode bias relative to the ground, increase distances and minimise the risk of electron emission by polishing and smoothing all the components facing the gun assembly in the dangerous regions. Even though calculations do not point to a discharge between the anode electrode and the first drift tube, two different designs have been foreseen as shown in Fig. 16.

4.3. Cathode data

The custom made cathode is produced by HeatWave Labs, Inc. The material is a mixture of BaO, CaO and Al_2O_3 with a ratio of 6:1:2, and for stability against sputtering the surface is impregnated with Sc_2O_3 [28]. For an operation temperature of 1000 °C the current density limit in the thermionic emission regime is j_e=3 A/cm^2 - well above the 1 A/cm^2 required to reach an emission current of 1 A. The concave emitting surface has a curvature radius of 10 mm. In order to minimise stray magnetic fields produced by the cathode heater, the cathode is heated by a bifilar heater. The supply and return wires are connected to a central lead at the rear of the cathode and the base plate itself, respectively. The heat conduction between the cathode and its base is minimised by their main connection being a thin-wall MoRe tube.

5. Introduction of carbon

Carbon can be introduced into the EBIS either as a singly charged ion beam from an external primary ion source, or as a neutral gas. The former one is preferential for radioactive carbon isotopes where efficiency is a crucial aspect [29]. For stable isotopes neutral molecular carbon can be injected directly into the EBIS via a gas inlet close to the trapping region. Carbon oxides are absorbed by the NEG and therefore non-optimal. Injection of CH_4 or C_2H_4 is preferential because the carbon hydrates are not absorbed by the NEG [30]. In addition, the hydrogen has a cooling effect on the carbon ions inside the ionisation region owing to the mass difference between the ion species.

In order to meet the requirements for linac-based LIT the EBIS would have to deliver 10^8 C^{6+} ions per pulse at a repetition rate of 400 Hz. We assume an ion extraction efficiency of 50% and that only 50% of the primary CH_4^+ ions reach the highest charge state by the end of the breeding time (2.5 ms). Given that all CH_4 to CH_4^+ ionisations happen in a 100 mm segment of the trapping region inside the electron beam, which has a radius of 60 μm, then the necessary ionisation rate per volume is λ_{C+}=1.4·10^{20} s^{-1}m^{-3}. We have here assumed that the CH_4^+ will after further ionisation dissociate and the charged carbon ions will stay trapped in the electron beam. At an electron density of j_e=3.5 kA/cm^2 and an electron impact ionisation cross-section of σ=1.65·10^{-17} cm^2 for $CH_4 \rightarrow CH_4^+$ at 9 keV electron energy [31], the required particle density results in N=λ_{C+}·e/(σ·j_e)=3.9·10^{14} m^{-3}, or 1.6·10^{-8} mbar.

To maintain a reasonable vacuum inside the EBIS while enhancing the ionisation probability in the central trapping region, we suggest the use of a gas cell. It could be realised as a tube that substitutes one of the drift tubes (see Fig. 18). Unlike the regular drift tubes, which are perforated for better pumping, the gas cell has a closed cylindrical surface equipped with a gas inlet at its centre and apertures on both axial sides for differential pumping. The gas inlet is a tube of 3 mm inner diameter that is electrically insulated from the gas cell in order not to disturb its functionality as a drift tube. For such a geometry of a 100 mm gas cell with 6 mm apertures, the CH_4 pressure distribution inside the EBIS was calculated with the software Molflow+ [32] and the result is shown in Fig. 18. For production of the required amount of ions within the gas cell, 9.2·10^{-7} mbar·l/s CH_4 has to be injected via the gas inlet, corresponding to roughly 3·10^{12} molecules per second. Outside the gas cell the pressure drops down to the 10^{-10} mbar range.

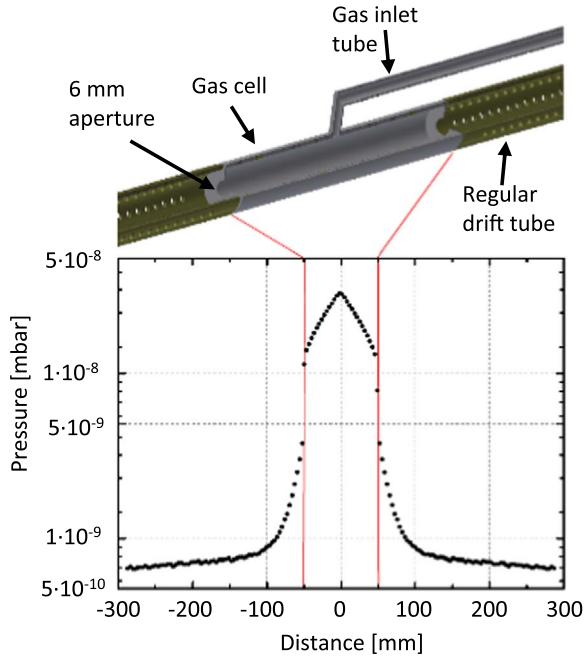

Fig. 18. Gas cell with adjacent drift tubes and gas inlet tube. The gas cell is 100 mm long, has 6 mm apertures on both axial ends and has the same inner diameter as the regular drift tubes. Below the CH_4 pressure distribution in the trapping region inside the EBIS is shown. The abscissa shows the axial distance from the gas inlet, which is located at the centre of the 100 mm long gas cell, and in the centre of the trapping region.

6. Conclusion and outlook

The design of a high-compression Brillouin-type electron gun has been completed. Inserted in an EBIS with a solenoidal field strength of at least 2 T it should fulfil carbon-ion production specifications given by 2nd generation IBT facilities, i.e. is 10^8 C^{6+} per pulse with a repetition rate of 400 Hz. The specifications translate into an electron current of 1 A at a beam energy of 7.5–10 keV and a current density of at least 1.5 kA/cm^2, inside a trapping region of approximately 25 cm length.

Electron beam simulations have addressed traditional gun characteristics, such as perveance (calculated to 1 μAV$^{-1.5}$) and beam compression, but also several second-order effects. For example, side-emission of electrons from the cathode and methods to mitigate it have been studied. Thermal effects were included to assess the reduction in effective electron current density inside the trapping region, and the result agree with Hermann's formula. The risk of magnetic mirror reflection in the solenoid gradient due to the transverse momentum was also evaluated, showing that for a well aligned electron gun reflections will only occur at solenoidal field strengths exceeding 5.8 T. Three-dimensional simulations have provided handles on acceptable mechanical tolerances, and the axial alignment of the cathode with respect to the Wehnelt electrode appears to be especially crucial with a tolerable displacement of about ±50 μm.

The gun design is based around an innovative conception of the Wehnelt electrode. The Wehnelt piece is in fact a ceramic insulator, providing the isolation between the cathode and the anode. A molybdenum coating on part of the surface constitutes the actual Wehnelt electrode. This construction minimises the risk of mechanical alignment errors between cathode and anode, and assures as well a good alignment of the magnetic field in the crossover point. The magnetic field profile can be adjusted by a smaller internal gun coil inside and an anode coil outside the iron shield. The electron emitting cathode will be of dispenser type and operate at 1 A/cm^2, well below the expected maximal emission current of 3 A/cm^2, at an operational temperature of 1273 K. The large margin should guarantee a minimal influence on the effective transverse electron beam energy caused by local fluctuations in the work function.

We have shown that if carbon is introduced into the EBIS in the form of CH_4, the required flow rate and pressure are acceptable from an EBIS operational point-of-view, provided the injection is done into a semi-closed gas cell surrounding the electron beam in the trapping region.

The gun is to be tested at the TwinEBIS setup at CERN, which has a 2 T solenoid. The initial tests will focus on the electron gun performance and the electron beam optics. At a later stage ion extraction could be foreseen if the setup is complemented with an ion-extraction line. Provided the electron loss current is low during the tests it would thereafter be of interest to try MEDeGUN in a 5 T solenoid in order to exploit its full performance. If the operational characteristics and long-term reliability of the electron gun are good, one could consider adapting the REXEBIS charge breeder for the MEDeGUN design.

Acknowledgments

We would like to acknowledge M. Delonca for mechanical stress calculations and A. Pikin for general advice. The MEDeGUN project is supported by a dedicated grant provided by the CERN Knowledge Transfer fund. Author J. Pitters is supported by a Marie Skłodowska-Curie Innovative Training Network Fellowship of the European Commission's Horizon 2020 Programme under contract number 642889 MEDICIS-PROMED.

References

[1] H. Tsujii, T. Kamada, A review of update clinical results of carbon ion radiotherapy, Jpn. J. Clin. Oncol. 42 (2012) 670–685. http://dx.doi.org/10.1093/jjco/hys104.
[2] H. Eickhoff, U. Linz, Medical applications of accelerators, Rev. Accel. Sci. Technol. 1 (2008) 143–161. http://dx.doi.org/10.1142/S1793626808000083.
[3] A. Peeters, et al., How costly is particle therapy? Cost analysis of external beam radiotherapy with carbon-ions, protons and photons, Radiother. Oncol. 95 (2010) 45–53. http://dx.doi.org/10.1016/j.radonc.2009.12.002.
[4] Y.Iwata, et al., Present status of a superconducting rotating-gantry for carbon therapy, in: Proceedings of HIAT 2015, Yokohama, pp. 288–290, ⟨http://accelconf.web.cern.ch/AccelConf/HIAT2015/papers/frm1c01.pdf⟩, 2015.
[5] K. Tasaki, et al., Development of HTS magnet for rotating gantry, Phys. Procedia 81 (2016) 162–165. http://dx.doi.org/10.1016/j.phpro.2016.04.041.
[6] A. Shornikov, F. Wenander, Advanced electron beam ion sources (EBIS) for 2-nd generation carbon radiotherapy facilities, J. Instrum. 11 (2016) T04001. http://dx.doi.org/10.1088/1748-0221/11/04/T04001.
[7] U. Amaldi, A.Degiovanni, Proton and carbon linacs for hadron therapy, in: Proceedings of the Linear Accelerator Conference (LINAC) 2014, Geneva, p. FRIOB02. [Online]. jacow.org/LINAC2014/papers/friob02.pdf, 2014.
[8] A. Garonna, et al., Cyclinac medical accelerators using pulsed C6+/H2+ ion sources, Jour. Instr. 5 (9) (2010) C09004. http://dx.doi.org/10.1088/1748-0221/5/09/C09004.
[9] S. Verdú-Andrés, et al., Literature review on linacs and ffags for hadron therapy, Int. J. Mod. Phys. A 26 (10–11) (2011) 1659–1689. http://dx.doi.org/10.1142/S0217751×11053109.
[10] U. Amaldi, et al., High frequency Linacs for Hadrontherapy, Rev. Accel. Sci. Technol. 2 (2009) 111–131. http://dx.doi.org/10.1142/S179362680900020X.
[11] R. Becker, et al., Simulation of charge breeding for trapped ions, J. Phys.: Conf. Ser. Vol. 58 (2007) 443–446. [Online]. ⟨http://iopscience.iop.org/1742-6596/58/1/102⟩.
[12] R.Becker, et al., The EBIS option for hadron therapy, in: Proceedings of the EPAC 98 proceedings, pp. 2345–2347. [Online]. ⟨http://accelconf.web.cern.ch/AccelConf/e98/PAPERS/WEP09C.PDF⟩, 1998.
[13] M.V. Nezlin, Physics of Intense Beams in Plasmas, CRC Press, 1993. [Online]. ⟨https://books.google.ch/books?id=rQN3lPMdIGMC & printsec=frontcover#v=onepage & q & f=false⟩.
[14] A. Shornikov, et al., Parametric study of a high current–density EBIS charge breeder regarding two stream plasma instability (TSI), Nucl. Instr. Meth. B 376 (2016) 361–363. http://dx.doi.org/10.1016/j.nimb.2015.12.008.
[15] A. Pikin, et al., Simulation and optimization of a 10A electron gun with electrostatic compression, Rev. Sci. Instr. 84 (2013) 033303. http://dx.doi.org/10.1063/1.4793773.
[16] Y.V. Baryshev, et al., A 100 MW electron source with extremely high beam area compression, Nucl. Instr. Meth. A 340 (1994) 241–258. http://dx.doi.org/10.1016/0168-9002(94)90100-7.
[17] G.R. Brewer, Focusing of high-density electron beams, Focusing of charged

particles 2, Academic Press, New York and London, 1967, p. 73 (ISBN 978-0-12-636902-1).
[18] R. Mertzig et al., Electron Beam Simulation from Gun to Collector, Towards a Complete Solution, In: Proceedings of the AIP Conf. Proc., vol. 1640, 2015, pp. 28-37. [Online]. http://dx.doi.org/10.1063/1.4905397.
[19] A. Pikin et al., First Test of BNL Electron Beam Ion Source with High Current Density Electron Beam, in: Proceedings of the AIP Conf. Proc., vol. 1640, 2015, pp. 12-18. [Online]. http://dx.doi.org/10.1063/1.4905395.
[20] S. Humphries, TRAK charged particle tracking in electric and magnetic fields, in: Proceedings of the AIP Conf. Proc., vol 297, 1993, pp. 597-604. [Online]. http://dx.doi.org/10.1063/1.45318.
[21] E.P. Lee, R.K. Cooper, General envelope equation for cylindrically symmetric charged-particle beams, Part. Accel. 7 (1976) 83–95. [Online]. ⟨http://cds.cern.ch/record/1107845/files/p83.pdf⟩.
[22] G.I. Kuznetsov, Cathodes for electron guns, Physica Scr. vol T71 (1997) 39–45. http://dx.doi.org/10.1088/0031-8949/1997/T71/007.
[23] K.T. Compton, Electrical discharges in gases, 1st. ed., Electrical Discharge 4, Pergamon press, 1961, pp. 326–393 (ISBN978-1-4831-9909-2. [Online]. ⟨http://www.sciencedirect.com/science/book/9781483199092⟩.
[24] W.D. Kilpatrick, Criterion for vacuum sparking designed to include both rf and dc, *Rev. Sci. Inst.* 28 (1957) 824–826. http://dx.doi.org/10.1063/1.1715731.
[25] M. Breitenfeldt, et al., The TwinEBIS setup: machine description, Nucl. Instrum. Methods Phys. Res. A 856 (2017) 139–146. http://dx.doi.org/10.1016/j.nima.2016.12.037.
[26] ⟨http://www.ansys.com/⟩.
[27] K. Wasa, Handbook of Sputter Deposition Technology: fundamentals and Applications for Functional Thin Films, Nano-Materials and MEMS, William Andrew, Waltham, 2012 (ISBN 978-1-4377-3483-6).
[28] HeatWave Labs, Inc., Document TB-119, ⟨http://www.cathode.com/pdf/TB-119.pdf⟩.
[29] R.S. Augusto, et al., New developments of 11C post-accelerated beams for hadron therapy and imaging, Nucl. Instr. Meth. B 376 (2016) 374–378. http://dx.doi.org/10.1016/j.nimb.2016.02.045.
[30] K. Welch, Capture pumping technology, 2-nd fully revised edition, Elsevier, 2001 (ISBN 0-444-50882-1).
[31] B.L. Schramm, et al., Absolute gross ionization cross sections for electrons (0.6-12 keV) in hydrocarbons, Jour. Chem. Phys. 44 (1966) 49–54. http://dx.doi.org/10.1063/1.1726502.
[32] R. Kersevan, J.-L. Pons, Introduction to MOLFLOW+: new graphical processing unit-based Monte Carlo code for simulating molecular flows and for calculating angular coefficients in the compute unified device architecture environment, J. Vac. Sci. Technol. A 27 (2009) 1017–1023. http://dx.doi.org/10.1116/1.3153280.